Supplementary Information (SI) for Journal of Materials Chemistry A.

Supplementary Materials for

High-Efficiency Frost and Ice Control *via* Sensing-Assisted Nanovibrational Slippery Surfaces

Yuchen Shen[1†], Dylan Boylan[1†], Fangying Chen[1†], Feng Guo[2], Meiying He[1], Xianming Dai[1*]

[1]Department of Mechanical Engineering, University of Texas at Dallas, 800 W Campbell Rd, Richardson, TX 75080

[2]Department of Intelligent Systems Engineering, Indiana University Bloomington, 107 S Indiana Ave, Bloomington, IN 47405

†These authors contributed equally to this work

*Corresponding Author

Email: Dai@utdallas.edu

Table of Contents

List of Figures and Tables

Supplementary Notes

Supplementary Figures

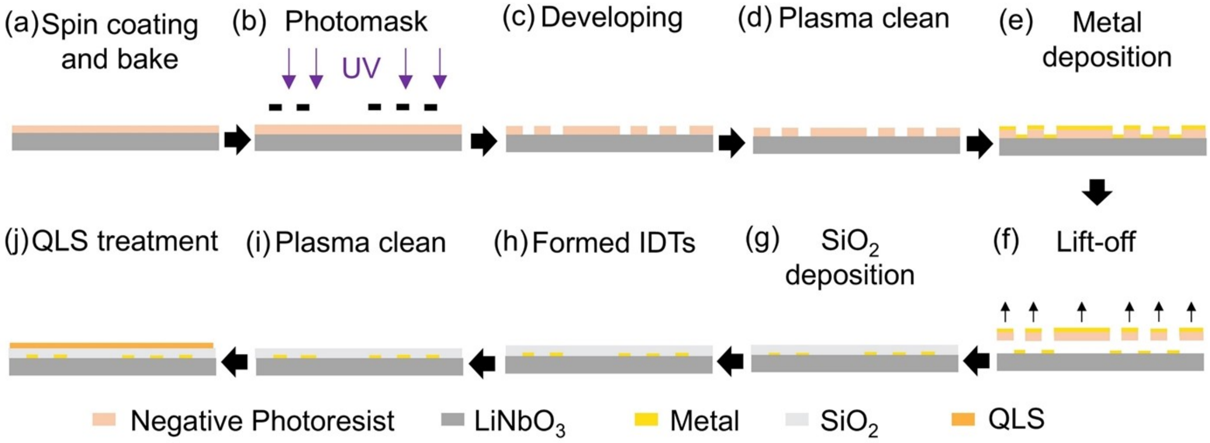

Figure S1. Fabrication of the sensor-assisted nanovibrational device with QLS treatment.

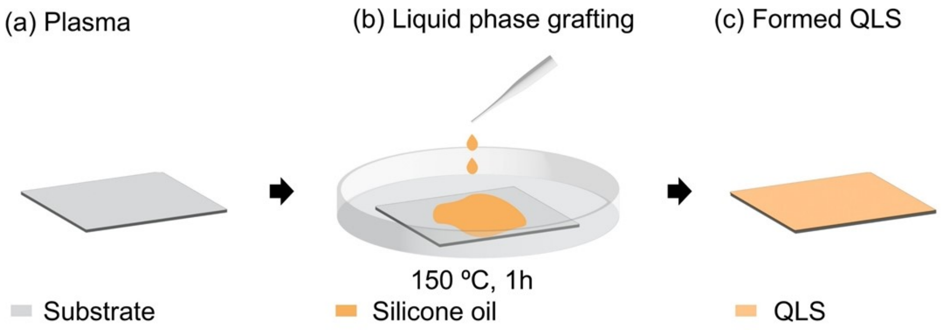

Figure S2. Surface treatment to form QLS

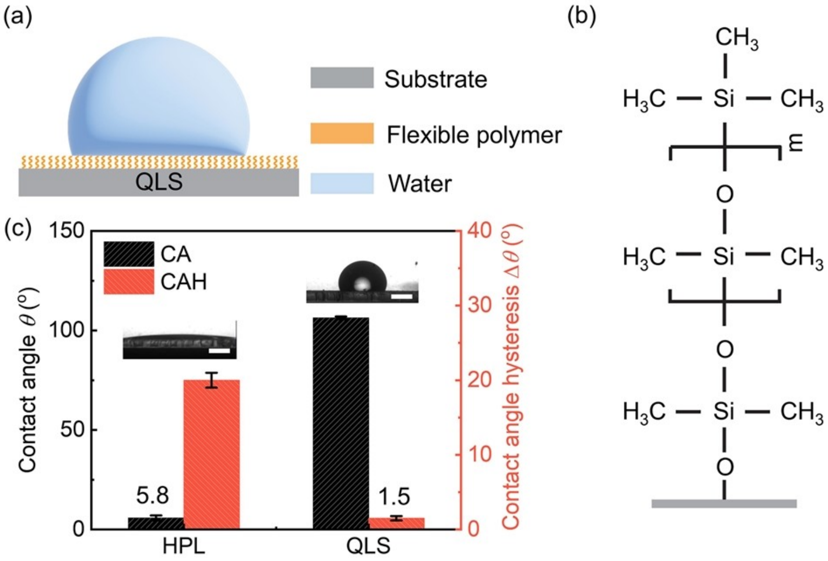

Figure S3. Surface morphology and contact angle measurement. (a) Schematic diagram of a water droplet on QLS surface. (b) Chemical structure of polymer grafting on QLS. (c) Contact angle measurement of QLS and hydrophilic surface. Scale bar is 1 mm.

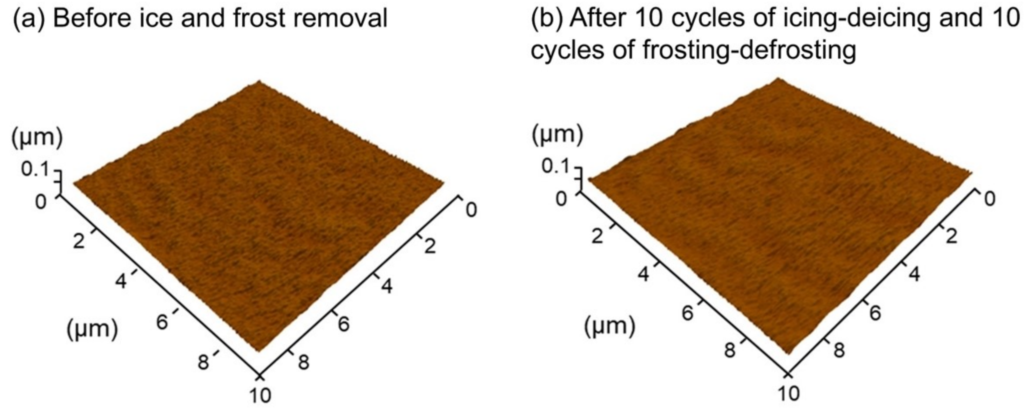
(a) Before ice and frost removal

(b) After 10 cycles of icing-deicing and 10 cycles of frosting-defrosting

Figure S4. Roughness measurements through atomic force microscopy (AFM) for QLS. R_{RMS} = 0.5 nm for both samples.

Atomic force microscopy (AFM) measurements for QLS surfaces were carried out in tapping mode using a multimode microscope (Jupiter XR, Asylum Research). At least 3 independent measurements were taken for each coating.

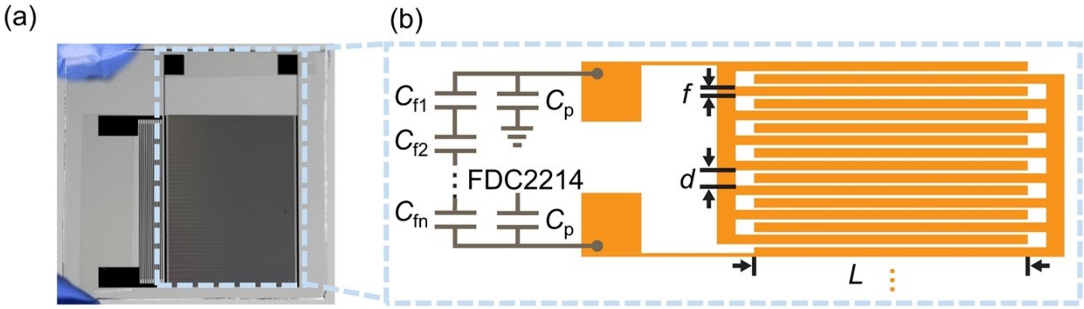

Figure S5. Design of the capacitive sensor. (a) Image of the device. Left: acoustic IDTs; right: capacitive sensor electrodes. (b) Schematic diagram of the capacitive sensor electrodes.

The capacitive sensing element consists of interdigitated electrodes (IDEs) fabricated adjacent to the acoustic interdigital transducers (IDTs) on the device substrate (Fig. S5). The IDE structure employs a parallel-finger configuration with optimized geometric parameters to maximize the sensing performance. The capacitive sensor features 105 pairs of electrodes with a finger width (f) of 50 µm and finger spacing on one side (d) of 100 µm, spanning an active sensing length (L) of 15.6 mm. This configuration was designed to achieve optimal capacitive coupling while maintaining fabrication feasibility. The sensing mechanism relies on the capacitance between adjacent electrode fingers ($C_{\text{f1}}...C_{\text{fn}}$), which forms the active sensing element of the device. Each pair of fingers contributes to the measurement capacitance, with the total sensing capability determined by the cumulative effect of all finger pairs. The device also exhibits parasitic capacitance (C_{p}) arising from external factors such as electrical connections, wiring, and peripheral circuitry. These parasitic effects were carefully considered in the design process to ensure optimal sensor performance. A capacitance-to-digital converter (FDC2214, Texas Instruments Incorp.) was integrated into the system for capacitance measurements with a frequency of 50 Hz.

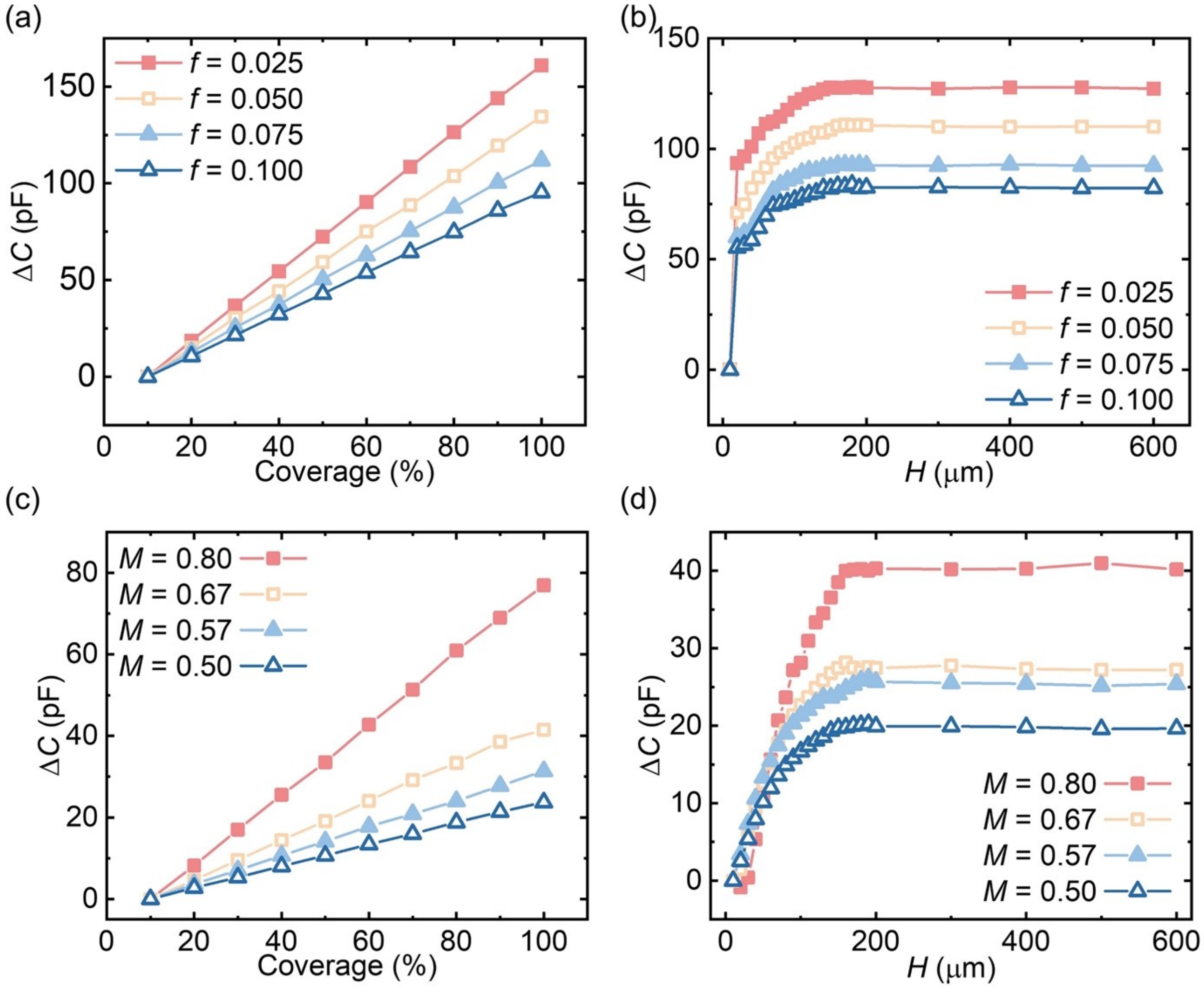

Figure S6. Sensor optimizations. (a) Simulated capacitance change (ΔC) versus surface coverage percentage for different finger width (Unit: mm). (b) ΔC as a function of water height (H) for varying finger width (Unit: mm). (c) ΔC versus surface coverage percentage for different metallization ratios. (d) ΔC as a function of water height for varying metallization

The geometric parameters of the capacitive sensor were optimized through finite element analysis using *COMSOL Multiphysics* Electrostatics interface. The simulation employed Maxwell's equations with emphasis on the electric potential distribution ($\nabla^2 V = -\rho/\varepsilon$) and capacitive coupling between electrodes. Water ($\varepsilon_r = 80$) was used as the target material to evaluate the performance of the sensor, simulating practical sensing conditions. The electrostatic field distribution was solved using a quasi-static approximation, with the metallic electrodes modeled as perfect electrical conductors.

Two key geometric parameters were investigated: the metallization ratio $M = 2f/(d+f)$, The capacitance change (ΔC) was evaluated by systematically varying two parameters: the water coverage percentage over the electrode surface and the water height (H) above the electrodes. As shown in Fig. S6a, smaller finger size (f) (0.025-0.100 mm) resulted in higher sensitivity, with $f =$ 0.025 mm achieving the maximum capacitance change of approximately 160 pF at 100% water coverage. Similarly, Fig. S6b demonstrates that the water height (H) exhibits a saturation behavior beyond 200 μm for all finger widths, indicating the effective sensing range of the device. The impact of metallization ratio (M) was studied in parallel (Fig. S6c and Fig. S6d), revealing that higher M values (0.80) provided enhanced sensitivity, with a maximum ΔC of approximately 40 pF at $H = 200$ μm. However, the final design parameters ($f = 50$ μm, $M = 0.67$) were selected as an optimal compromise between maximum sensitivity and practical fabrication constraints, particularly considering the minimum feature size limitations of conventional photolithography processes. The chosen configuration ensures robust sensor performance while maintaining reliable fabrication yield.

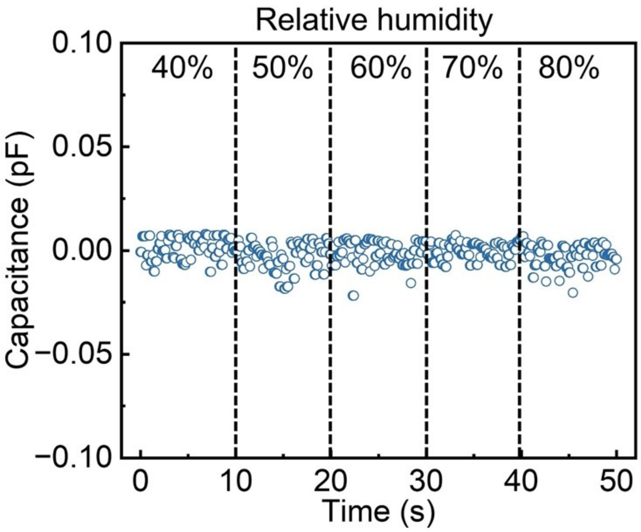

Figure S7. Stability of the capacitive sensor under varying humidity conditions.

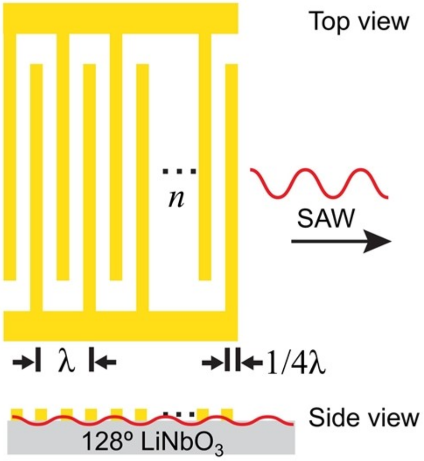

Figure S8. Design of the acoustic IDTs

Surface acoustic waves (SAWs) were generated using an interdigital transducer (IDT) fabricated on 128° rotated Y-cut X-propagating lithium niobate ($LiNbO_3$) substrate. The IDTs were designed for 10 pairs of fingers with a wavelength (λ) of 300 µm, corresponding to a theoretical resonant frequency of 13.26 MHz based on the substrate's acoustic velocity (3978.2 m/s)[1]. This optimized finger size and spacing enables efficient electromechanical coupling, resulting in the generation of strong acoustic waves[2]. The actual operating frequency was optimized to 13.36 MHz to achieve maximum performance, with the slight deviation attributed to material imperfections and fabrication tolerances. Each IDT consisted of periodically spaced electrodes with a width of $\lambda/4$ (75 µm), maintaining the standard finger-to-gap ratio of 1:1 for optimal electromechanical coupling.

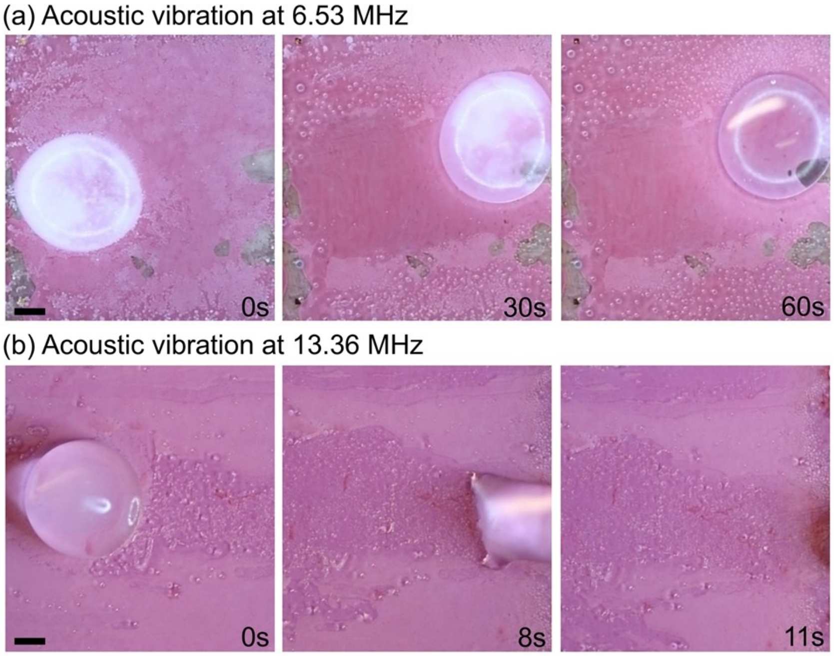

Figure S9. Comparison of ice removal performance at different SAW frequencies. Scale bar = 1 mm.

This figure shows the experimental comparison between SAW devices operating at 6.53 MHz and 13.36 MHz under the same input power. The higher-frequency device achieves complete droplet removal within 11 seconds, while the lower-frequency device fails to remove the melted water, demonstrating the enhanced acoustic force and efficiency at 13.36 MHz. Supplementary video 7 shows the dynamic removal of this process.

(a) Acoustic vibration with 100 mVpp amplitude

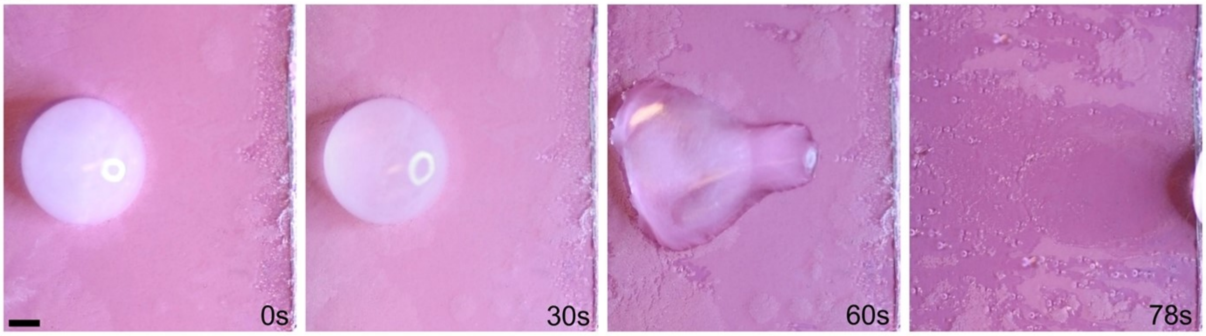

(b) Acoustic vibration with 200 mVpp amplitude

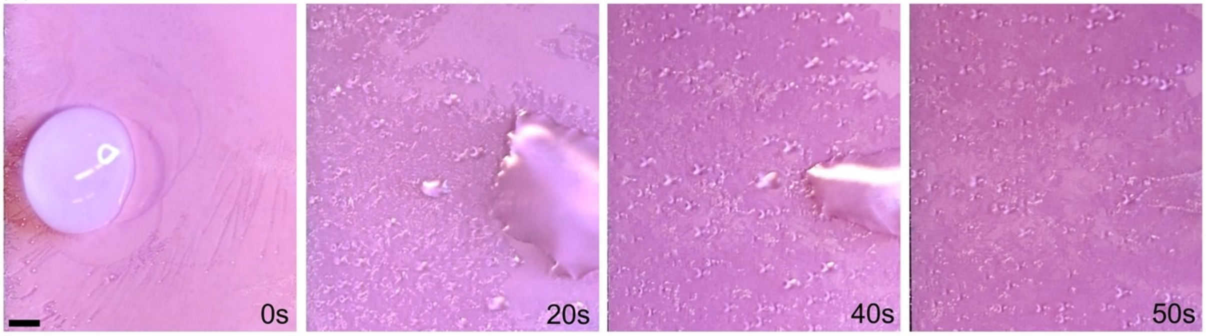

(c) Acoustic vibration with 300 mVpp amplitude

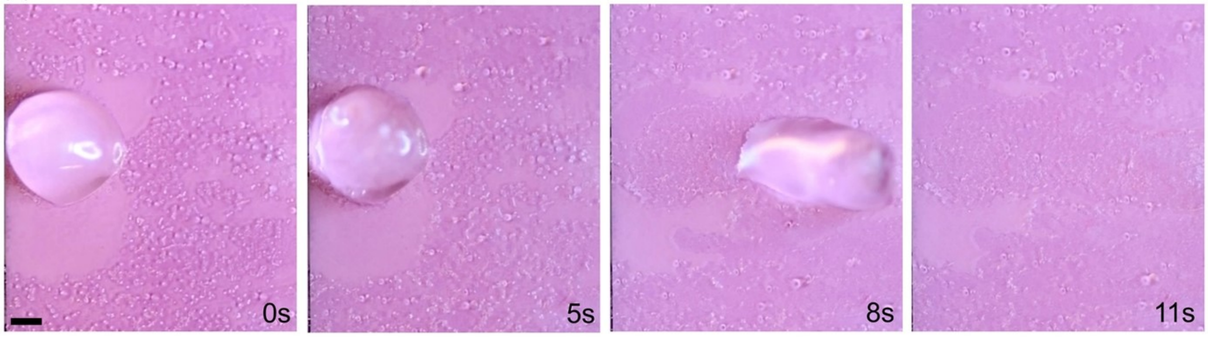

Figure S10. Effect of actuation amplitude on SAW-driven ice removal performance. Scale bar = 1 mm.

This figure presents the effect of varying input amplitudes (100 mVpp, 200 mVpp, and 300 mVpp) at a fixed frequency of 13.36 MHz. Higher amplitudes produce stronger acoustic forces and faster ice removal.

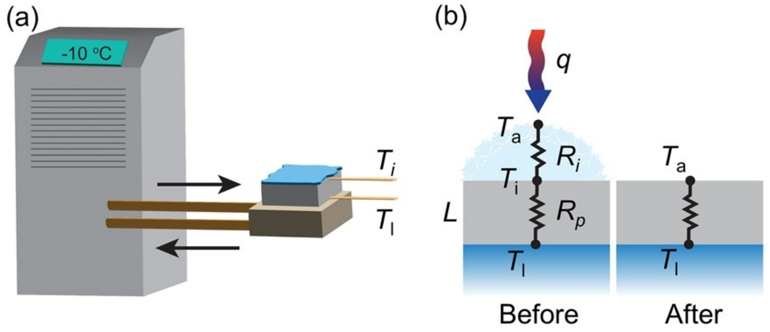

Figure S11. Heat flux measurement and thermal resistance network. (a) Schematic diagram of the heat flux measurement setup. (b) Thermal resistance network before and after frost removal

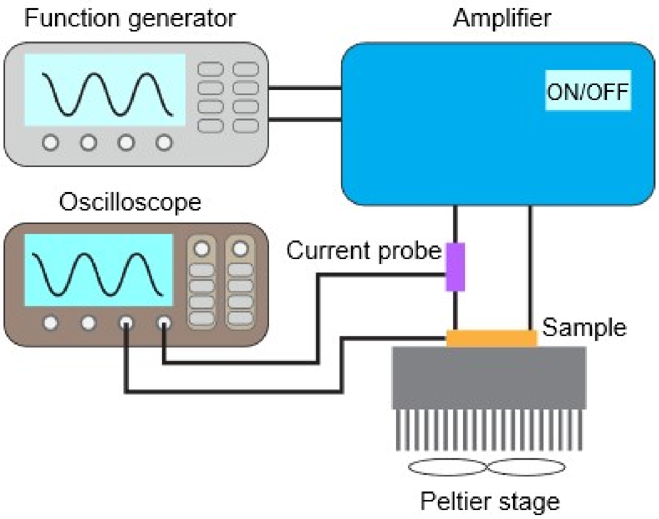

Figure S12. Experimental setup for condensate, ice and frost removal. The system consists of a function generator providing input signals, connected to an amplifier that powers the SAW device. A current probe and oscilloscope are used to measure energy consumption. The sample is placed on a Peltier stage maintained at 5°C for condensate formation and -10°C for ice and frost formation studies.

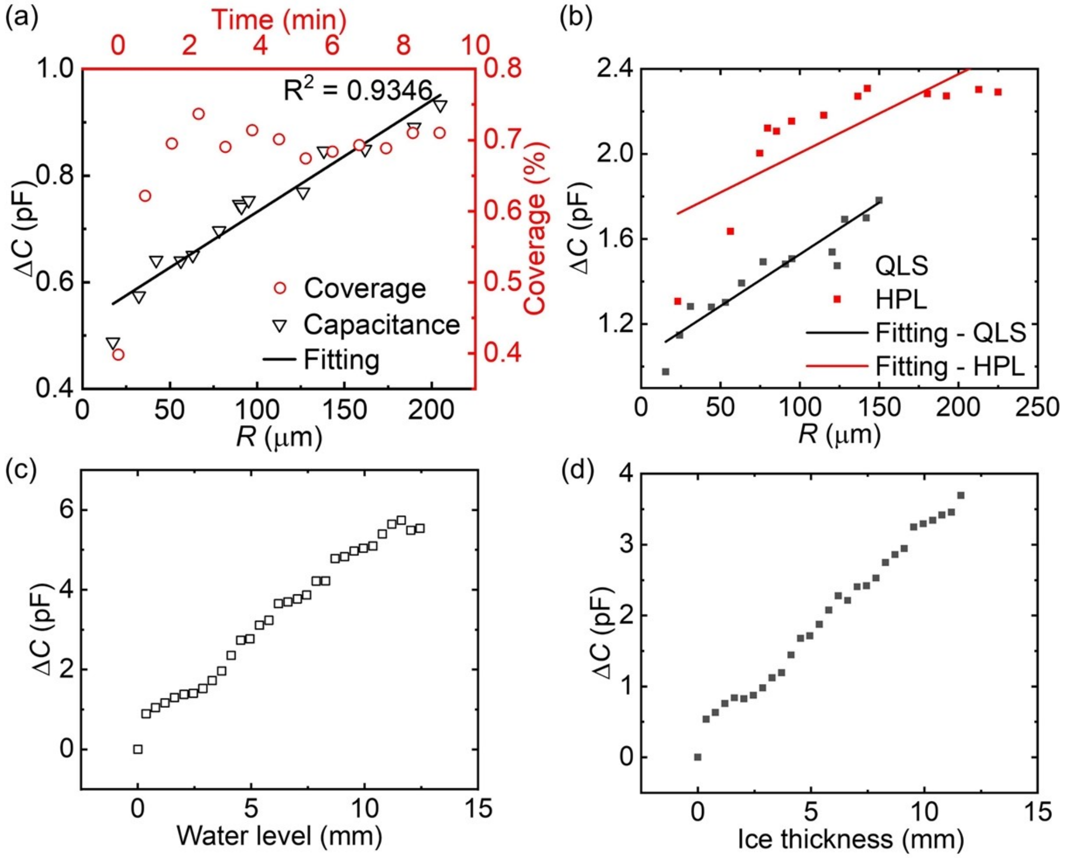

Figure S13. Sensor calibration. (a) Correlation between capacitance change (Δ*C*) and droplet radius (*R*) on a quasi-liquid surface (QLS). Black triangles and line show capacitance measurements and linear fit, respectively. Red circles indicate surface coverage evolution over time (right axis). (b) Comparative analysis of Δ*C* versus *R* on QLS and hydrophilic surface (HPL). Solid lines represent linear fits for each surface condition. (c) Calibration curve showing Δ*C* as a function of uniform water level height. (d) Relationship between Δ*C* and ice layer thickness.

We performed comprehensive calibration of our capacitive sensor under various water/ice conditions to validate its detection capabilities. The sensor response was characterized by both dropwise condensation and uniform layer coverage scenarios. The coverage ratio was captured by a camera and calculated by image processing.

For dropwise condensation, measurements were conducted on two distinct surfaces: a quasi-liquid surface (QLS) and a hydrophilic surface (HPL). On the QLS (Fig. S13a), the capacitance change (Δ*C*) showed a strong linear correlation (R^2 = 0.9346) with droplet radius (*R*), while the surface coverage rapidly stabilized around 0.7% within the first 2 minutes. This suggests that after initial nucleation, the capacitance change is predominantly influenced by droplet growth rather than coverage expansion. The hydrophobic nature of QLS ensures consistent droplet geometry, contributing to the reliable linear relationship. In contrast, measurements on the HPL surface (Fig. S13b) exhibited greater variation in the ΔC-R relationship. This deviation from linearity can be attributed to the variable droplet morphology on the hydrophilic surface, where drops tend to spread irregularly rather than maintain consistent contact angles.

For uniform coverage scenarios, we examined both liquid water and ice layers. The sensor demonstrated a near-linear response to increasing water levels (Fig. S13c) and ice thickness (Fig. S13d), confirming its capability to quantitatively monitor both phase states.

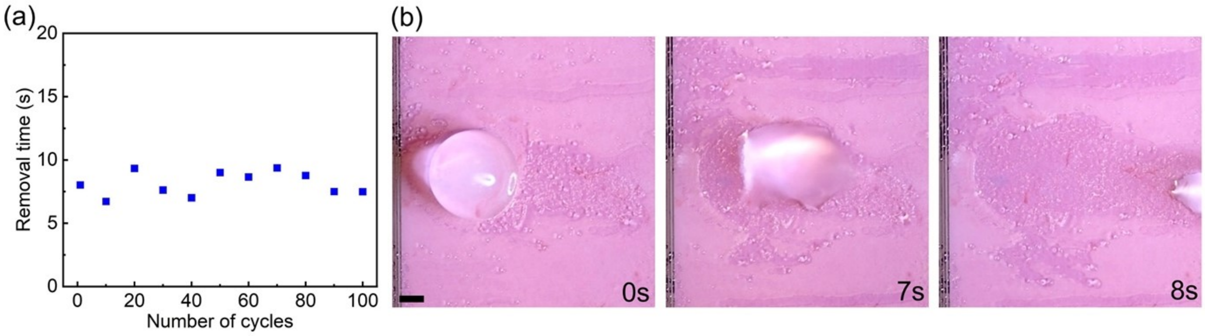

Figure S14. Durability evaluation of ice removal performance over 100 icing/deicing cycles using 20µl water. (a) Ice removal time across 100 icing/deicing cycles. (b) Ice removal process at cycle #100. Scale bar = 1 mm.

Supplementary Table

Supplementary Table 1. Relative permittivity of air, water and ice[3]

Materials	Air	Water	Ice
Relative permittivity	1	80	56.9

Supplementary Note 1. Energy consumption analysis

The removal energy consumptions of frost and ice were calculated as follows,

For Joule heating:

(per unit volume)
$$E_{r,heat} = \rho_i \cdot \left[c_i (0 - T_i) + L_m + T_v \cdot c_w + L_v \right] \tag{S1}$$

in which ρ_i is the density of ice/frost, c_i and c_w is the specific heat of ice and water, T_i is the ice/frost temperature, T_v is the steam temperature, L_m and L_v is the latent heat of melting and vaporization.

For SAW actuation (SAW as the only source), the energy consumption was calculated based on the measured power and operation time in Eq. S9 to Eq. S11.

During the ice and frost removal under SAW, there are residues left after actuation, particularly on hydrophilic surface. In such case, the residues were assumed to be removed by Joule heating (named 'Heating + Nanovibration'), and the total energy consumption is,

$$E_r = E_{r,SAW} + \rho_w \cdot V_r \cdot \left[(T_v - T_w) c_w + L_v \right] \tag{S2}$$

in which $E_{\mathrm{r,\,SAW}}$ is the SAW actuation energy consumption, ρ_w is the density of water, V_r is the volume of the water residues, T_w is the water temperature.

The daily defrosting energy consumption (Fig. 4d and Fig. 4e) was estimated based on the experimental data for condensate removal. The energy intensity for SAW removal (ϕ_SAW) was calculated as follows,

$$\phi_{SAW} = P_{in} / S \tag{S3}$$

in which P_in is the input power from SAW, S is the condensation surface area. Based on the temperature data, when the difference of air and dew point temperature (T_a - T_dew) is less than 8°C, it indicates that the condensation will form on the heat pump outdoor unit surfaces (assuming surface temperature is 8°C lower than air temperature). We estimate the time with the condensate (t_c) and measured P_in at 500 mVpp, burst mode. Therefore, the total energy consumption is sum of the rectangular areas (Fig. 4d, bottom). Meanwhile, we calculated the mass per unit area (M_c) of condensate based on our experiment during t_c, and the energy intensity for Joule heating (ϕ_heat) is calculated as,

$$\phi_{heat} = M_c \left[c_w (T_v - T_w) + L_v \right] \tag{S4}$$

Assuming in Joule heating, the defrosting operates every 6 hours for 30 min, the total energy consumption is the sum of the four rectangular areas in Fig. 4e.

Supplementary Note 2: Mechanism of droplet removal induced by SAW

During the condensation process, we observed distinct droplet behavior patterns under surface acoustic wave (SAW). Initially, microscale condensate droplets exhibited nanovibrational motion while remaining anchored to the surface, with some droplets coalescing with their neighbors (Supplementary Video 1). As condensation progressed and droplets grew through both direct condensation and coalescence events, the influence of the acoustic wave became more pronounced. Notably, once droplets reached a critical size, they were rapidly removed from the surface. This size-dependent removal mechanism is primarily driven by acoustic streaming effects, with the streaming force becoming increasingly dominant as droplet size increases. In smaller droplets, the streaming force appears insufficient to overcome surface adhesion, resulting only in droplet nanovibration. However, as droplets grow, the interaction area with the streaming field increases, potentially leading to stronger shear and lift forces that can overcome surface adhesion. While acoustic radiation forces may contribute to this process, our observations suggest that streaming effects play the predominant role in droplet removal, particularly given the localized fluid motion patterns around the droplets (Fig. 3a). Considering the retention force at the solid-liquid interface, the net force balance determines whether the droplet will remain stationary or undergo directed motion along the substrate surface.

Droplet streaming

When a Rayleigh SAW encounters a liquid medium on the substrate surface, it experiences attenuation due to the leakage of acoustic energy into the fluid (Fig. S15a). This leaky SAW phenomenon results in a longitudinal wave radiating into the liquid at the Rayleigh angle θ_{Ra}, while simultaneously creating a pressure wave that drives fluid motion[4]. The Rayleigh angle is given by[5]:

$$\theta_{Ra} = \sin^{-1}\frac{V_L}{V_R}, \tag{S5}$$

where V_{L} and V_{R} are the velocities of the longitudinal wave in the liquid and SAW. The leaky SAW is attenuated as it propagates along the substrate beneath the liquid, with the leaked energy serving as a source of acoustic streaming. The SAW streaming force in the fluid can be expressed as[4]:

$$\vec{f}_s = -\rho(1+\alpha_1^2)^{3/2} A^2 \omega^2 k_i \exp 2(k_i x + \alpha_1 k_i z)\,, \tag{S6}$$

in which ρ is the droplet density, α_1 is the attenuation coefficient, A is the amplitude of the SAW, ω is the angular frequency and k_i is the wavenumber of the leaky SAW. The positions x and z represent the tangential and normal coordinates, respectively, relative to the origin located at the point of incidence where the surface acoustic wave (SAW) interacts with the droplet on the device surface. Here, $\vec{f}_s$ is the net force per unit volume, considering the entire droplet on a surface, the total force can be expressed as:

$$F_s = \frac{\pi R^3}{3}(1-\cos\theta_c)^2(2+\cos\theta) f_s\,, \tag{S7}$$

in which R is the droplet radius, θ_c is the droplet contact angle.

Retention force

The retention force (F_r) opposing droplet motion arises from contact angle hysteresis at the liquid-solid interface (Fig. S15b). Contact angle hysteresis manifests as the difference between the advancing contact angle (θ_A) and receding contact angle (θ_R) that develop at the leading and trailing edges of the droplet, respectively. When a droplet is subjected to SAW streaming force on a horizontal surface, this hysteresis creates a resistive force that must be overcome to initiate droplet motion. The retention force can be expressed as[6]:

$$F_r = \gamma D(\cos\theta_R - \cos\theta_A)\,, \tag{S8}$$

where γ is the liquid-air surface tension, D is the droplet base diameter of the liquid droplet, θ_R is the receding contact angle, θ_A is the advancing contact angle.

The magnitude of the retention force varies significantly with surface properties. On a conventional hydrophilic surface, the substantial difference between θ_A and θ_R results in a strong retention force that resists droplet motion. In contrast, on a quasi-liquid surface (QLS), the nature of the slippery surface dramatically reduces contact angle hysteresis (θ_A - θ_R) (Fig. S3c), leading to a much smaller retention force. This reduction in contact angle hysteresis on QLS explains why droplets can be moved more easily on such surfaces, requiring less SAW streaming force to initiate and maintain motion.

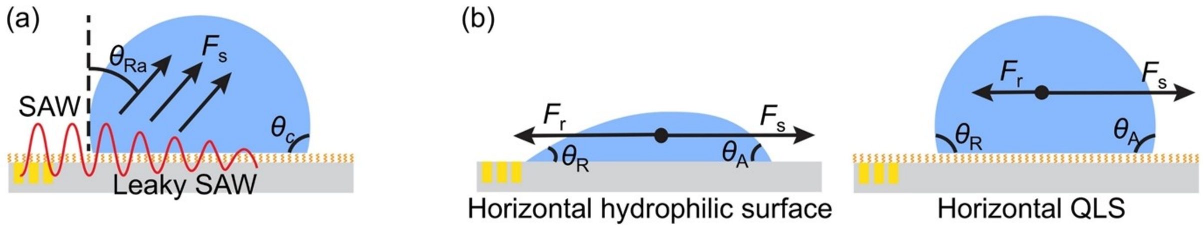

Figure S15: Forces analysis of a droplet on a surface under SAW. (a) SAW streaming force applied on the droplet, induced by the leaky SAW. (b) Comparison of the retention force on the droplet on hydrophilic and QLS surfaces.

Droplet motion criteria

Droplet motion under SAW excitation occurs when the SAW streaming force (F_s) exceeds the retention force (F_r). Two key scaling relationships determine this force balance: 1) The SAW streaming force scales with the cube of droplet radius ($F_s \propto R^3$) while the retention force scales linearly with radius ($F_r \propto R$), resulting in that large droplets can be easily removed; 2) The streaming force exhibits quadratic dependence on wave amplitude ($F_s \propto A^2$), indicating that increased input power significantly enhances droplet mobility while retention force remains constant.

Supplementary Note 3. SAW actuation modes for condensate, frost, and ice removal

Surface acoustic wave (SAW) actuation was implemented using two primary modes: full (continuous) mode and Burst (pulse) mode. In Full actuation mode, SAW excitation is applied constantly to the substrate, providing uninterrupted acoustic energy input. In contrast, burst mode operates in cycles consisting of 3 ms actuation periods followed by 7 ms rest intervals - this specific timing was determined through optimization experiments testing various burst periods, with this combination showing superior removal performance. The burst mode enables higher instantaneous nanovibration amplitudes while reducing average power consumption and unnecessary heat to ice/frost, as the “off” periods allow the system to dissipate heat more effectively, preventing excessive temperature rise. For ice removal, we additionally employed a hybrid “full-burst” mode, which begins with 20 seconds of continuous actuation followed by burst mode operation (Fig. S16a), combining the thermal benefits of continuous heating with the mechanical advantages of high-amplitude pulsed actuation.

For frost removal, both QLS (quasi-liquid-shedding) and HPL (hydrophilic) surfaces were tested under full and burst mode actuation. The residual mass measurements in Fig. S16b demonstrate that QLS surfaces consistently show superior performance, with residuals below 0.2 g for both actuation modes compared to >0.4 g for HPL surfaces. Burst mode operation achieves slightly better removal efficiency (approximately 15% lower residuals) while maintaining reduced energy consumption, as evidenced by the SAW removal energy E_r measurements in Fig. S16c.

The full-burst mode demonstrates particular effectiveness for ice removal applications. As shown in Fig. S16c, while both full and full-burst modes successfully remove ice from QLS surfaces, the full-burst mode achieves this with approximately 25% lower energy consumption (E_r). The enhanced performance of full-burst mode can be attributed to its two-phase operation:

1) Initial full actuation phase (20s): Provides consistent heating to melt the ice-substrate interface, weakening the adhesion between ice and surface

2) Subsequent burst phase: Delivers high-amplitude acoustic forces that effectively dislodge the partially melted ice while minimizing overall energy consumption

The combination of these phases optimizes both the thermal and mechanical aspects of ice removal. The full mode component ensures sufficient interfacial melting, while the burst mode component provides stronger instantaneous removal forces due to its higher peak amplitude, resulting in more efficient removal with lower total energy input. The energy consumption data in Fig. S16c demonstrates the superior efficiency of burst and full-burst modes across all removal scenarios. The removal energy was calculated as following,

Full mode:
$$E_r = P_{in} \times t_r \tag{S9}$$

Burst mode:
$$E_r = P_{in} \times t_r \times \frac{n}{N} \tag{S10}$$

Full – Burst mode:
$$E_r = P_{in} \times \left[t_i + (t_r - t_i) \times \frac{n}{N} \right] \tag{S11}$$

in which P_{in} is the input power from SAW, t_{r} is the removal time, n is the burst cycle (n = 40080 in 3 ms), N is the total cycle in one period (N = 133600 in 10 ms) and t_{i} is the duration of the initial Full actuation for Full-Burst mode. The SAW power P_{in} was obtained by the measurements of the voltage and current through the device (Fig. S12).

For both ice and frost removal, these modes achieve comparable or better removal times (t_{r}) while consistently requiring lower removal energy (E_{r}). This efficiency gain is particularly pronounced in ice removal applications, where full-burst mode reduces energy consumption by approximately 25% compared to full mode while maintaining equivalent removal effectiveness.

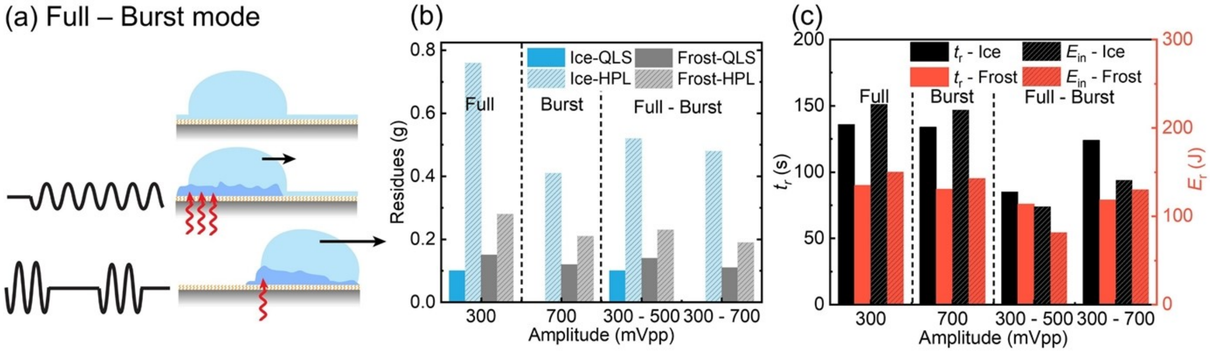

Figure S16. Comparison of surface acoustic wave (SAW) actuation modes. (a) Schematic illustration of full-burst mode operation, showing the waveform patterns for continuous and burst actuation. The burst mode consists of 3 ms actuation followed by 7 ms rest periods. (b) Residual mass measurements comparing ice and frost removal on hydrophilic and QLS surfaces, and under different actuation modes and amplitudes. (c) Removal time (t_{r}) and SAW removal energy (E_{r}) comparison between ice and frost removal under different actuation modes and amplitudes on QLS.

Supplementary Note 4. Mechanism of ice and frost removal induced by SAW

Under SAW excitation, frost and ice exhibit distinct removal behaviors. For frost removal, we observe a progressive process along the SAW propagation direction where the frost first melts at the SAW entry point, creating a liquid waterfront (Fig. S17a). This water accumulates at the boundary between the melted and unmelted regions, advancing forward as more frost melts, until all frost is transformed into water and transported away from the surface. In contrast, ice removal follows a different pattern: SAW energy first induces melting at the ice-substrate interface, forming a thin water layer beneath the bulk ice. Subsequently, the entire ice structure, together with the underlying water layer, is removed from the surface as a combined unit (Fig. S17b). These distinct behaviors can be attributed to three main mechanisms: the thermal-mechanical effects of SAW that initiate and drive the removal process, the acoustic radiation force that acts differently on frost crystals versus bulk ice, and the scale-dependent drag forces.

Primary thermal and mechanical mechanisms

The distinct removal mechanisms stem from how SAW energy interacts with these different structures. For frost removal, SAW energy generates localized heating at the frost-substrate interface, initiating melting. The resulting water is then transported forward by SAW-induced acoustic streaming and surface tension gradients. This accumulated water enhances heat transfer to adjacent frost regions, creating a progressive melting front that continues until complete removal is achieved. Ice removal, however, relies on SAW energy concentrating at the ice-substrate interface, causing localized melting at the base. The formation of a thin water layer reduces ice-substrate adhesion, allowing SAW forces to displace the entire ice-water mixture as a unit.

Streaming and drag force

Surface acoustic waves generate streaming flow patterns that play a crucial role in the removal of both frost and ice formations through distinct mechanisms[7]. In frost removal, the streaming forces first interact with the frost layer at the SAW entry point, where the acoustic energy creates a localized melting effect. As the frost melts into liquid water or small ice crystals, these particles become susceptible to the streaming flow. However, the process is initially constrained by the presence of unmelted frost ahead, which acts as a physical barrier. The streaming forces continue to drive the melting front forward while simultaneously generating drag forces that transport the melted material. The progressive nature of this mechanism ensures systematic frost removal along the SAW propagation direction.

For ice removal, the mechanism primarily operates through the formation of a thin water layer at the ice-substrate interface. The streaming forces generated by SAW create this interfacial water layer, which significantly reduces the adhesion between the ice and the substrate. Once this water layer is established, the streaming flow produces sufficient drag force to mobilize the entire ice structure as a single unit. The combination of reduced friction at the interface and the sustained drag force from the streaming flow facilitates efficient bulk ice removal. While acoustic radiation forces[8] may contribute to both frost and ice removal processes, the streaming-induced drag forces serve as the primary driving mechanism for the observed removal patterns.

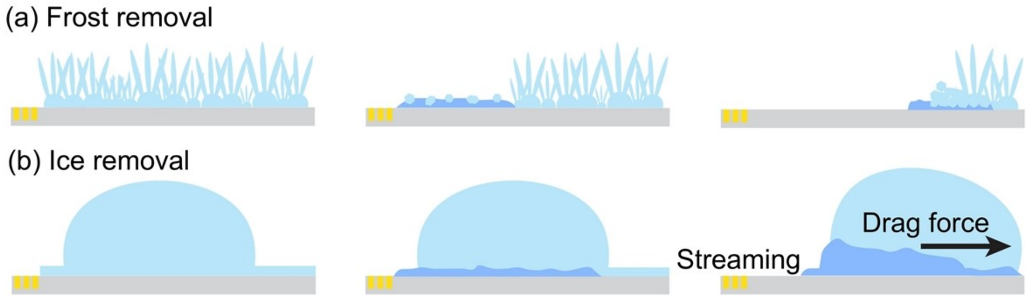

Figure S17. Mechanism of Ice and Frost Removal by SAW. (a) Schematic illustration of ice removal process: initial state (left), formation of confined liquid layer with acoustic radiation force (F_{rad}) and drag force (F_{d}) (middle), and subsequent removal of bulk ice (right). (b) Sequential process of frost removal: initial frost structure (left), melting and formation of liquid front (middle), and progressive removal of melted frost.

References

1. G. Kovacs, M. Anhorn, H. Engan, G. Visintini and C. Ruppel, 1990.
2. F. Guo, Z. Mao, Y. Chen, Z. Xie, J. P. Lata, P. Li, L. Ren, J. Liu, J. Yang and M. Dao, *Proc. Natl. Acad. Sci. U.S.A.*, 2016, **113**, 1522-1527.
3. A. Von Hippel, *IEEE Trans. Dielectr. Electr. Insul*, 1988, **23**, 801-816.
4. S. Shiokawa, Y. Matsui and T. Ueda, *Jpn. J. Appl. Phys.*, 1990, **29**, 137.
5. H. Song, D. Jang, J. Lee, K. Y. Lee and S. K. Chung, *J. Micromech. Microeng.*, 2021, **31**, 125007.
6. C. Furmidge, *J. Colloid Sci.*, 1962, **17**, 309-324.
7. M. Ishikawa, T. Hirata and T. Fujii, *Int. J. Refrig* 2002, **25**, 208-217.
8. G. Torr, *Am. J. Phys.*, 1984, **52**, 402-408.